

Nanoparticle Redistribution in PC3 Tumors Induced by Local Heating in Magnetic Nanoparticle Hyperthermia: In Vivo Experimental Study

Qimei Gu

Department of Mechanical Engineering,
University of Maryland-Baltimore County,
Baltimore, MD 21250

Tejashree Joglekar

Department of Biology,
University of Maryland-Baltimore County,
Baltimore, MD 21250

Charles Bieberich

Department of Biology,
University of Maryland-Baltimore County,
Baltimore, MD 21250

Ronghui Ma

Department of Mechanical Engineering,
University of Maryland-Baltimore County,
Baltimore, MD 21250

Liang Zhu¹

Department of Mechanical Engineering,
University of Maryland-Baltimore County,
1000 Hilltop Circle Baltimore,
Baltimore, MD 21250
e-mail: zliang@umbc.edu

In magnetic nanoparticle hyperthermia, a required thermal dosage for tumor destruction greatly depends on nanoparticle distribution in tumors. The objective of this study is to conduct in vivo experiments to evaluate whether local heating using magnetic nanoparticle hyperthermia changes nanoparticle concentration distribution in prostatic cancer (PC3) tumors. In vivo animal experiments were performed on grafted PC3 tumors implanted in mice to investigate whether local heating via exposing the tumor to an alternating magnetic field (5 kA/m and 192 kHz) for 25 min resulted in nanoparticle spreading from the intratumoral injection site to tumor periphery. Nanoparticle redistribution due to local heating is evaluated via comparing microCT images of resected tumors after heating to those in the control group without heating. A previously determined calibration relationship between microCT Hounsfield unit (HU) values and local nanoparticle concentrations in the tumors was used to determine the distribution of volumetric heat generation rate (q'''_{MNH}) when the nanoparticles were subject to the alternating magnetic field. SAS, MATLAB, and EXCEL were used to process the scanned data to determine the total heat generation rate and the nanoparticle distribution volumes in individual HU ranges. Compared to the tumors in the control group, nanoparticles in the tumors in the heating group occupied not only the vicinity of the injection site, but also tumor periphery. The nanoparticle distribution volume in the high q'''_{MNH} range ($>1.8 \times 10^6$ W/m³) is 10% smaller in the heating group, while in the low q'''_{MNH} range of $0.6\text{--}1.8 \times 10^6$ W/m³, it is 95% larger in the heating group. Based on the calculated heat generation rate in individual HU ranges, the percentage in the HU range larger than 2000 decreases significantly from 46% in the control group to 32% in the heating group, while the percentages in the HU ranges of 500–1000 and 1000–1500 in the heating group are much higher than that in the control group. Heating PC3 tumors for 25 min resulted in significant nanoparticle migration from high concentration regions to low concentration regions in the tumors. The volumetric heat generation rate distribution based on nanoparticle distribution before or after local heating can be used in the future to guide simulation of nanoparticle redistribution and its induced temperature rise in PC3 tumors during magnetic nanoparticle hyperthermia, therefore, accurately predicting required thermal dosage for safe and effective thermal therapy. [DOI: 10.1115/1.4042298]

Keywords: magnetic nanoparticle hyperthermia, nanoparticle redistribution, heating, bioheat, theoretical model

1 Introduction

In recent years, nanoparticle hyperthermia has been demonstrated to enhance wave energy absorption (laser photothermal therapy and ultrasound) and to confine energy generation (magnetic nanoparticle hyperthermia) in tumors to minimize collateral tissue damage. In magnetic nanoparticle hyperthermia, magnetic nanoparticles delivered to the tumor site can generate heat when subject to an alternating magnetic field [1–5]. Once the nanoparticles are manufactured, the induced volumetric heat generation rate subject to a specific magnetic field and thermal dosage required to damage the tumor are primarily dependent on the concentration distribution of nanoparticles in the tumor.

Various studies have been performed to design hyperthermia treatment protocols to not only achieve an effective thermal dosage to targeted tumor, but also minimize collateral thermal damage to surrounding healthy tissue. With the advancement in computational resources, one can also design an individualized treatment plan tailored for actual tumor size and shape based on scanned images, as well as implement precise nanoparticle distribution into the heat transfer model [6–7]. Typically, via the Pennes bioheat equation [8], transient temperature field of targeted tumor regions can be simulated with known local blood perfusion rate and volumetric heat generation rate distribution. A thermal damage model can be incorporated into the temperature field to assess permanent thermal damage to tumor cells.

One important factor in heat transfer simulation is temperature response of the vasculature to external and internal effects. In a living system, blood flow rate and vessel size may change as a response to local temperature, local pH value, and local O₂ and CO₂ levels. On the other hand, any change in local blood perfusion rate can significantly alter the local temperature field, since

¹Corresponding author.

Contributed by the Heat Transfer Division of ASME for publication in the JOURNAL OF HEAT TRANSFER. Manuscript received June 4, 2018; final manuscript received December 11, 2018; published online January 14, 2019. Assoc. Editor: Bumsoo Han.

the local blood perfusion rate usually acts as a heat sink to carry heat away from the targeted hyperthermia region. During heating treatment, the local blood perfusion rate in tumors is thought to increase due to regulation of local factors to dilate blood vessels [9]. However, the extent of the increase in blood perfusion rate in tumors is typically smaller than that of normal tissues, due to lack of smooth muscle in tumor vasculature that prevents compensatory vasodilation. This feature has been suggested for inducing preferential thermal damage to tumors because a high thermal dosage in tumors can be maintained due to its weak ability of carrying heat away from the tumor region. Once the heating is prolonged, the tumor blood flow decreases progressively, partially due to thermal damage to the blood vessels in the tumor region. In theoretical simulation of temperature fields of tumors in hyperthermia treatment, most previous studies have incorporated dynamic responses of local blood perfusion rate into the bioheat equation, typically with a temperature-dependent local blood perfusion rate to model the early increase and later decrease in blood perfusion rate [10–12]. Although it would have been ideal to have real-time measurements of local blood perfusion as an input to the Pennes bioheat equation, it is still a challenge to implement it in clinical settings and some of the imaging approaches such as magnetic resonance imaging lack required spatial and temporal resolutions and are also costly. Nevertheless, employing temperature-dependent local blood perfusion rate improves the simulation accuracy in heating process in tumors. In previous studies by our group, we generated a tumor model with nanoparticle distribution from microCT scans and assumed the temperature-dependent local blood perfusion rate during heating [13]. All tumors disappeared from the site in later animal experiments using the designed heating protocol, suggesting accuracy of the theoretical simulation including dynamic responses of local vasculature to heating [14].

One limitation of the previous theoretical simulations of tumor temperature field is the assumption of unchanged nanoparticle distribution during heating. With a direct intratumoral injection of ferrofluid into tumors, the spreading of nanoparticles is dominated by the high pressure at the injecting needle tip as the driving force. Once the injection stops, previous experiments using transparent tissue equivalent agarose gels have shown that the nanoparticle distribution had no noticeable change several hours after the injection. Although local nanoparticle concentration is not uniform, the driving force due to nanoparticle diffusion may not be adequate to overcome other barriers to smooth out the nonuniform concentration field. However, once a tumor undergoes local heating, it is possible that nanoparticle distribution would change due to damaged tumor region. In fact, previous clinical studies have demonstrated a more uniform temperature elevation field in tumors when the tumors were heated repeatedly [15]. It is possible that local heating alters the porous structure that further results in changes in transport properties in tumors, such as tumor porosity and nanoparticle diffusion coefficient. Cell death may lead to an increase in interstitial space. The extracellular matrix may also be damaged during heating to allow reduction in flow resistance. Therefore, nanoparticles, initially more concentrated in the vicinity of the injection site, may diffuse to the less concentrated region due to a decrease in diffusion resistance by the increased nanoparticle diffusion coefficient. Another possibility of dispersing nanoparticles may be driven by the release of intracellular fluid during heating. Local heating elevates tissue temperature, which in turn, may result in disruption of cell membrane and cell death. The originally bound intracellular fluid, once released, may elevate local pressure and provide a driving force for the migration of nanoparticles. Further, it has been suggested that cell damage may lead to a reduction in solid tissue stress and further decrease interstitial fluid pressure in tumors [16]. In term of theoretical simulation of temperature elevating in tumors, magnetic nanoparticle redistribution in tumors during heating would have altered the volumetric heat generation rate distribution, therefore, leading to different heating protocol designs to maximize tumor damage while minimizing collateral thermal damage to healthy tissue.

Although multiscale modeling approaches have been used to simulate nanoparticle transport in tumors during intratumoral injection and during heating, accuracy of the approaches requires detailed information of heterogeneous tumor structure and its dynamic responses to heating [17–20]. Experimental measurements of nanoparticle redistribution would provide evidence to be used in the future to validate theoretical simulation of nanoparticle transport. Our previous *in vivo* animal experiments have suggested possible change in nanoparticle distribution in tumors after heating [21]. Unfortunately, the nanoparticle redistribution was not statistically significant, due to uncontrollable and unrepeatable nanoparticle deposition patterns in tumors in that study. The heterogeneous tumor structure and high pressure-induced crack formation in the tumors also added uncertainty on the calculated results to draw concrete conclusions. A recent experimental study by our group tested the hypothesis in semitransparent agarose gels [22]. A commercially available ferrofluid containing magnetic nanoparticles was injected into tissue equivalent agarose gels, to study nanoparticle spreading in the gel. A high-resolution microCT imaging system was used to investigate the nanoparticle concentration distributions before and after the gel specimens were subjected to heating of 15 min induced by an alternating magnetic field. Using a diluted agarose gel and a slow injection rate to minimize crack formation, we found that the nanoparticle region was almost spherical. Magnetic nanoparticle heating induced by an alternating magnetic field for 15 min altered nanoparticle distribution in the same gel via pushing nanoparticles further away from the infusion site, resulting in a 26% increase in nanoparticle distribution volume [22]. It is not clear whether similar observation occurs in actual tumors during magnetic nanoparticle hyperthermia.

In this study, *in vivo* animal experiments were performed on PC3 tumors implanted in mice to investigate whether local heating via exposing the tumor to an alternating magnetic field (5 kA/m and 192 kHz) for 25 min resulted in nanoparticle migration from the original intratumoral injection site. Nanoparticle redistribution due to local heating was evaluated via comparing microCT images of resected tumors after heating to those in the control group without heating. A previously determined calibration relationship between microCT Hounsfield unit (HU) value and local nanoparticle concentration in the tumors was used to determine the distribution of volumetric heat generation rate when the nanoparticles were subject to an alternating magnetic field. Analyses were used to determine the total heat generation rate and the nanoparticle distribution volumes in individual HU ranges.

2 Methods and Material

2.1 PC3 Cell Line, Preparation, and Tumor Growth. The cell line selected for this study is human prostate cancer PC3 line. PC3 cell line has poorly differentiated characters, suggesting that the cells do not resemble the typical healthy cells found in particular location in the body, making them easy to segregate and quantify. PC3 cells have a high level of holoclones around 10% of total cell culture, and a colony-forming stem cell that has a higher growth potential than meroclones. It is expected that each injection has a high chance leading to tumor formation [23]. PC3 cells were cultured in Petri dishes and after several steps of trypsinization process, the cells were suspended with a concentration of 1×10^6 cells per 50 μ L (PC3) (R&D Systems, Minneapolis, MN). The mixture was then ready for injection.

Twenty-one Balb/c Nu/Nu male mice (30.2 ± 0.6 g) were purchased from the Jackson Laboratory (Bar Harbor, ME). To minimize unpredictability between different mice, the mice are inbred until the third generation mice are born. These mice are knockout mice that are immune-deficient to ensure that the xenograft cancer cells grow uninhibited. The prepared PC3 cell solution containing 5×10^6 cells was then injected into each flank of the mouse using a 27 gauge needle (Tuberculin Syringe w/Needle by BD, Fischer Scientific, Springfield, NJ). The tumor size was estimated using a Vernier caliper, and the growth of the tumor was monitored three

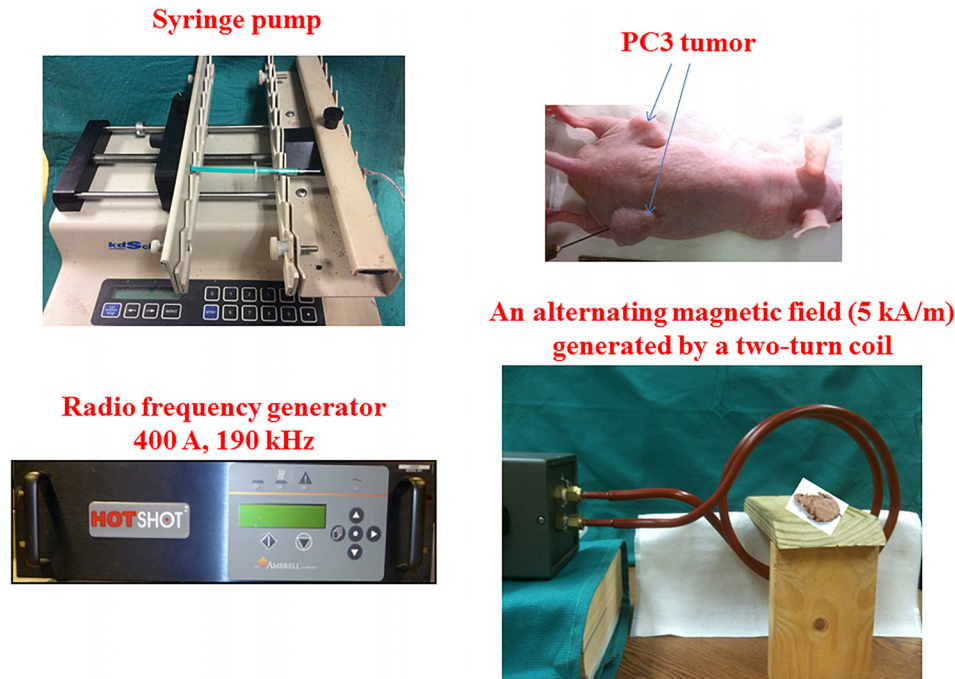


Fig. 1 Experiment setup consisting of a syringe pump for controlling infusion of ferrofluid, PC3 tumors implanted in mice, a radio frequency generator for inducing an alternating current, and generated alternating magnetic field

times a week until it reached 10 mm in the transverse diameter, which usually took 4–6 weeks [24].

2.3 Ferrofluid Infusion and Hyperthermia Treatment.

Once the tumor reaches a minimal size of 10 mm in the transverse diameter, the mouse was anesthetized by a sodium pentobarbital solution injection (40 mg/kg, i.p.). The mouse was then placed on a heating pad with circulating warm water to maintain normal body temperature of the mouse. The animal protocols have been approved by the University of Maryland Baltimore County Institutional Animal Care and Use Committee (IACUC).

A water-based ferrofluid (EMG 700, Ferrotec Corporation, Bedford, NH) with a volumetric concentration of 5.8% magnetite nanoparticles was used in this study. The EMG 700 nanoparticles have a nominal diameter of 10 nm with a log-normal standard deviation of approximately $\ln\sigma = 0.25$. The particles have been coated with an anionic surfactant to prevent particle agglomeration and displacement in the carrier fluid. The ferrofluid has a specific heat of 3979 J/kg·K, a density of 1290 kg/m³, a viscosity of less than 5 mPa·s at room temperature, and the saturation magnetization is 32.5 mT.

The experimental setup can be seen in Fig. 1. For each tumor, 0.1 cc of the ferrofluid was loaded into a 1 cc syringe (Norm-ject[®], Fischer Scientific, Springfield, NJ) and injected directly into the center of the tumor using a 26 gauge needle with a standard bevel tip (BD PrecisionGlide[™] needle, Fischer Scientific, Springfield, NJ). This injecting dosage delivers approximately 25.2 mg Fe to the tumor. The amount of the ferrofluid was decided based on our previous studies [7,13] to result in sufficient temperature elevations in tumors of similar sizes when subject to the same alternating magnetic field. The infusion rate was controlled by a syringe pump (Kd Scientific S230, Holliston, MA) and was selected as 3 μ L/min, the lowest rate used in our previous studies to result in the most repeatable and controllable nanoparticle deposition in PC3 tumors [7]. After the infusion, the needle tip was left inside of the tumor for 30 min to minimize any backflow through the needle track. Once the needle was removed, the mouse was allowed to rest for 30 min.

2.4 Heating Experiment. The mouse was then randomly placed in either the control group ($n=9$) or the heating group

($n=12$). The mouse in the heating group was placed in an alternating magnetic field for heating of 25 min. Showing in Fig. 1, a radio frequency (RF) generator was used to induce an alternating current of 200 A at a frequency of 192 kHz, passing through a two-turn coil to induce an alternating magnetic field at the center of the coil as 5 kA/m [7]. The mouse on the stage was adjusted so that the tumor was located at the center of the coil. The heating duration of 25 min was chosen to be the same as that in our previous experiments to induce maximal tumor damage [14]. After the heating, the tumor was dissected from the mouse and loaded in a microCT system for scan. The mouse in either group was then euthanized via sodium pentobarbital overdose (160 mg/kg, i.p.).

2.5 MicroCT Scan and Image Analysis. Each resected tumor was scanned using a high-resolution microCT system (SkyScan 1172, Micro Photonics, PA). The tumor was placed in a low-density Styrofoam container to minimize photon absorption and prevent movement of tumors during scanning. A tube of de-ionized water was included in each scan as a reference, so that the generated grayscale value can be converted into the standard Hounsfield unit scale, shown in Fig. 2. A power setting of 100 kV and 100 μ A with no filter was selected throughout the scan. This power setting allows for the greatest differentiation between the nanoparticles and the tumor tissue. Flat-field correction was used

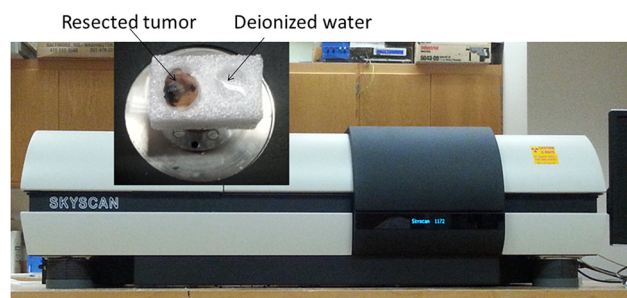


Fig. 2 A high-resolution microCT system to scan both a resected PC3 tumor and a specimen of de-ionized water

prior to each scan to minimize noise and artifacts. The addition of a ferrofluid into the tumor should result in brighter regions within the tumor tissue due to the increase in density by nanoparticles [7,21]. A medium resolution scan was used with a pixel size of $17.2 \mu\text{m}$. The scan time for each tumor was approximately 1 h, and each scan resulted in 800–1000 individual images depending on the actual tumor size.

The images were then reconstructed using the software NRECON provided by Micro Photonics. Before reconstruction, parameters such as ring artifacts, beam hardening, and smoothing were adjusted to minimize artifacts. The resultant reconstructed images are grayscale images where the pixel intensities range from 0 being black to 255 being white. The grayscale value depends on the X-ray source power level, type of X-ray source, filter, exposure time, and distance from the source to the object. To make the results by this study clinically relevant, they were converted into the Hounsfield unit, a standard unit of measurement for describing the radiodensity of a material [25]. On the Hounsfield unit scale, air has a value of -1000 , water has a value of 0 . Information from a tumor scan was then used to generate a linear relationship between the grayscale value and the HU value, based on the known HU values of air ($\text{HU}_{\text{air}} = -1000$) and water ($\text{HU}_{\text{water}} = 0$), as shown in the following expression:

$$\text{HU} = -1000 \frac{\text{GS} - \text{GS}_{\text{water}}}{\text{GS}_{\text{air}} - \text{GS}_{\text{water}}} \quad (1)$$

where GS is the grayscale value of the tested specimen at any pixel location, or water, or air in the microCT scans. Based on this relationship, the grayscale value (0–255) at any pixel location can be converted to the standard HU value.

2.6 Volumetric Heat Generation Rate and Deposited Heat Generation Rate in Tumors. Based on our previous experimental studies, we assume that the volumetric heat generation rate is proportional to the local nanoparticle concentration under a fixed magnetic field strength. Previous experiments [7] were performed to quantify the relationship between the q'''_{MNH} value and the nanoparticle concentration. Specifically, the magnetic nanoparticle solution used in the studies was mixed with agarose powder and phosphate-buffered saline solution to form specimens with known nanoparticle concentration. The specimen was placed in the same alternating magnetic field of 5 kA/m to induce heating, and q'''_{MNH} was determined by the initial temperature rise rate measured with a thermocouple [7]. The specimen was then scanned by the same microCT system to obtain its HU value. The following expression provides the relationship between the q'''_{MNH} value and HU value from the microCT images:

$$q'''_{\text{MNH}} = \begin{cases} 0 & \text{HU} < \text{HU}_{\text{threshold}} \\ q'''_{\text{specimen}} \frac{\text{HU} - \text{HU}_{\text{threshold}}}{\text{HU}_{\text{specimen}} - \text{HU}_{\text{threshold}}} & \text{HU} \geq \text{HU}_{\text{threshold}} \end{cases} \quad (2)$$

where $\text{HU}_{\text{threshold}}$ represents the Hounsfield unit of tumor tissue without nanoparticle. When the Hounsfield unit is lower than the threshold Hounsfield unit of tumor tissue without nanoparticles, no heat generation occurs and q'''_{MNH} is zero. Above this threshold, a linear relationship between q'''_{MNH} and the Hounsfield unit value has been observed, shown in Fig. 3. Our previous experimental study of the ferrofluid specimen at 5.8% volumetric concentration has an HU value of 2750. When the specimen is placed in the alternating magnetic field at 5 kA/m , the calculated volumetric heat generation rate q'''_{specimen} is found equal to $3.4 \times 10^6 \text{ W/m}^3$ [7]. As the same ferrofluid and magnetic field strength are used in this study, we use $\text{HU}_{\text{specimen}} = 2750$ and $q'''_{\text{specimen}} = 3.4 \times 10^6 \text{ W/m}^3$ in Eq. (2) to convert any microCT scan results to a distribution of q'''_{MNH} in the tumor. The generated q'''_{MNH} file can be used later to

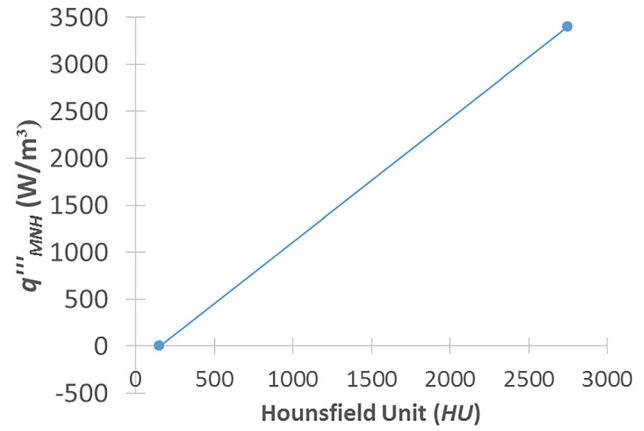


Fig. 3 The previously determined linear relationship between the q'''_{MNH} and microCT HU value

simulate temperature elevations in tumors subject to the same magnetic field in this study. The calculated Hounsfield unit $\text{HU}_{\text{threshold}}$ varies from one tumor to another, approximately around 100, similar to values reported previously [26]. The deviation of the calculated $\text{HU}_{\text{threshold}}$ from the Hounsfield unit of water ($\text{HU}_{\text{water}} = 0$) may be due to the fact that only 70% of the tumor tissue is water.

Once the q'''_{MNH} value is determined for each voxel volume, the energy generation rate (W) at that voxel is calculated by the multiplication of q'''_{MNH} and the voxel volume of $17.2^3 \mu\text{m}^3$, when the pixel size is $17.2 \mu\text{m}$. Using MATLAB, SAS, and EXCEL, one can then calculate the total energy rate deposited into the tumor q_{MNH} by adding the energy generation rates of all the voxel locations. This value, q_{MNH} , can be used to verify whether all the nanoparticles are deposited into each tumor. In theory, since all the tumors were injected with the same amount of the same ferrofluid, the total energy deposition rate in all the tumors should be similar. Further, the q'''_{MNH} information can also be used to evaluate heat generation contribution in specific ranges of HU values, via calculating the summation of the energy generation rates of the voxel locations in a specific range of HU. The information can be used to determine whether the nanoparticles are either spreading from the injection site or concentrated in the vicinity of the injection site.

2.7 Statistical Analyses. The results in individual groups are calculated and presented as mean \pm SD. Statistical evaluations between the control and heating groups were performed via both the Student's *t*-test the Wilcoxon rank sum test. One concern with using Student's *t*-test alone in this study is that the limited sample size may not guarantee a normal distribution. In light of this, the results were also evaluated using Wilcoxon rank sum test, a non-parametric analysis assuming unknown distribution. Statistically significant difference between two individual groups was confirmed when the *p*-value was less than 0.05.

3 Results

Based on the microCT images, the size of tumors can be calculated by the total number of voxels of tumor region. The tumors in both groups are similar in size (control: $1.28 \pm 0.12 \text{ cm}^3$, $n = 9$ versus heating: $1.27 \pm 0.10 \text{ cm}^3$, $n = 12$), calculated from the microCT scans via the total numbers of voxels and the known pixel size. Figure 4 gives the typical maximum intensity projection (MIP) images of PC3 tumors with an intratumoral nanoparticle injection. The presence of nanoparticles in tumors results in an elevation of the grayscale values, represented by the cloud in the images. MIP is a pseudo-3D visualization of the nanoparticles distribution in the tumor by projecting the maximum pixel intensity at each location to the foreground. The three images on the top row represent

Axial plane Sagittal plane Coronal plan

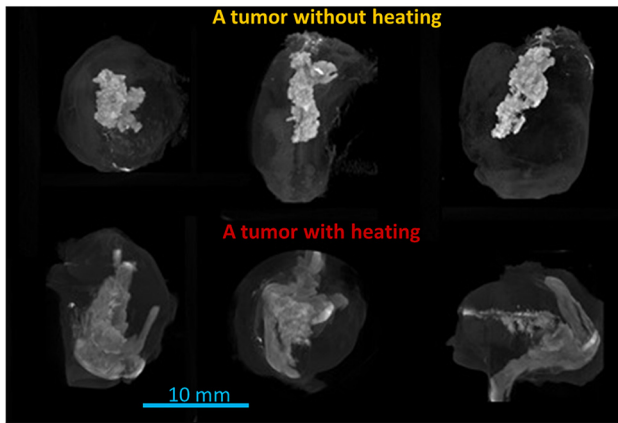


Fig. 4 Maximum intensity projection images of two tumors in the axial (left), sagittal (middle), and coronal (right) planes. The tumors were injected with 0.1 cc ferrofluid at an infusion rate of 3 mL/min, (top) a tumor in the control group without heating; and (bottom) a tumor in the heating group with 25 min of heating.

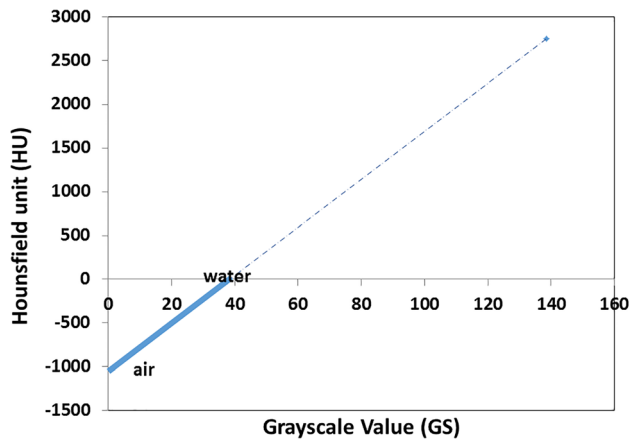


Fig. 5 Linear relationship between the Hounsfield unit and grayscale value in microCT scans, based on known HU values of air and de-ionized water. The dash line is an extension of the linear line to a wide range.

a tumor in the control group without heating. Similar to that in a previous study [7], the nanoparticles are deposited in the vicinity of the injection site (the tumor center). The bright white regions in the MIP images indicate areas containing highly concentrated nanoparticle deposition. The MIP images of a tumor after being heated for 25 min are shown in the bottom row of Fig. 4. Compared with the tumor without heating, nanoparticle deposition in

the heated tumor is quite irregular and one can see nanoparticle deposition also in the tumor periphery. The irregular paths of nanoparticle spreading may suggest formation of small cracks during heating, allowing originally confined nanoparticles to move to tumor periphery. Since all tumors were injected with the same amount of the ferrofluid, once the nanoparticles are spreading from the injection site to the periphery, the white cloud region appears less bright than that in the control group. It implies a lower local nanoparticle concentration in the tumors after heating.

Figure 5 shows a typical linear relationship between the microCT grayscale value and the HU value for the tumors. Note that the grayscale values of the air and water vary slightly from one scan to another. Using the HU value as an index of nanoparticle concentration, one can calculate the nanoparticle distribution volume defined as the combined volume of voxels within a specific HU range. Our results show that the average nanoparticle distribution volume in the heating group increases more than 42% ($p < 0.01$). Examining the nanoparticle distribution volume in specific HU ranges, one notes that the nanoparticle distribution volume in the high HU range >1500 is 10% smaller in the heating group, while in the low HU range of 500–1500, it is 95% larger in the heating group. As the different Hounsfield unit ranges represent individual nanoparticle concentrations, nanoparticles with lower concentrations occupy much bigger tissue volumes in the heating group than that in the control group.

Equation 2 has been used to convert the HU values of the microCT scans into q''_{MNH} . Each microCT slice image file may have a size larger than 75 MB, thus, analyzing all the microCT slices simultaneously would pose challenges to computational software. To reduce the size of the q''_{MNH} file, we averaged the q''_{MNH} values over a three-dimensional cluster of voxels. This greatly decreased the size of the q''_{MNH} file, while in the meantime it ensured that the amount of the total energy rate deposited in the tumor was not affected by the averaging procedures. In this study, we used a cluster having a volume of $12^3 \times 17.2^3 \mu\text{m}^3$ (12 pixels \times 12 pixels \times 12 pixels) to reduce the data size so that the software can handle.

Using this approach, the total energy generation rate deposited in each tumor can be calculated. The energy deposition rate ranges from 0.31 W to 0.43 W for all tumors. The total heat generation rates q_{MNH} in the tumors are found similar in both groups (control group: 0.35 ± 0.06 W versus heating group: 0.39 ± 0.03 W). The average value of the total heat generation rate in each group is very similar to that in our previous study (0.37–0.39 W) [7]. The results are expected due to the same infusion amount of ferrofluid used in both studies. It also suggests good control on minimizing ferrofluid leakage along the needle track as well as to the rest of the mouse body.

Since local nanoparticle concentration is assumed directly proportional to the local HU value, the total heat generation rate q_{MNH} is further divided into difference HU ranges: threshold-500, 500–1000, 1000–1500, 1500–2000, and above 2000. Table 1 lists the energy generation contribution of various nanoparticle concentration ranges. The HU range of threshold-500 is associated with a low local nanoparticle concentration with a local q''_{MNH} value varying from 0 to 0.5×10^6 W/m³, while the HU range ≥ 2000 represents a high local nanoparticle concentration or high

Table 1 Contributions of energy generation rates in both the control and heating group in individual HU ranges

HU range	Student's <i>t</i> -test			Wilcoxon rank sum test		
	Control group	Heating group	<i>p</i> -value	Control group (median)	Heating group (median)	<i>p</i> -value
Threshold-500	0.088 ± 0.016 W	0.102 ± 0.040 W	0.12	0.094 W	0.107 W	0.17
500–1000	0.045 ± 0.024 W	0.083 ± 0.023 W	0.001	0.037 W	0.082 W	0.001
1000–1500	0.023 ± 0.007 W	0.043 ± 0.014 W	0.0002	0.025 W	0.045 W	0.001
1500–2000	0.031 ± 0.011 W	0.039 ± 0.016 W	0.09	0.035 W	0.04 W	0.094
>2000	0.163 ± 0.046 W	0.127 ± 0.042 W	0.04	0.167 W	0.121 W	0.064

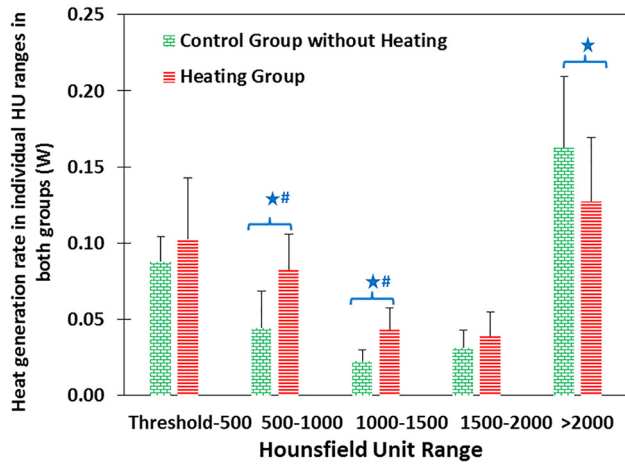


Fig. 6 Heat generation rate in individual HU ranges of tumors in both the control group without heating and the heating group. The symbol * (Student's *t*-test) or the symbol # (Wilcoxon rank sum test) denotes significant difference between the control and heating groups with a *p*-value less than 0.05.

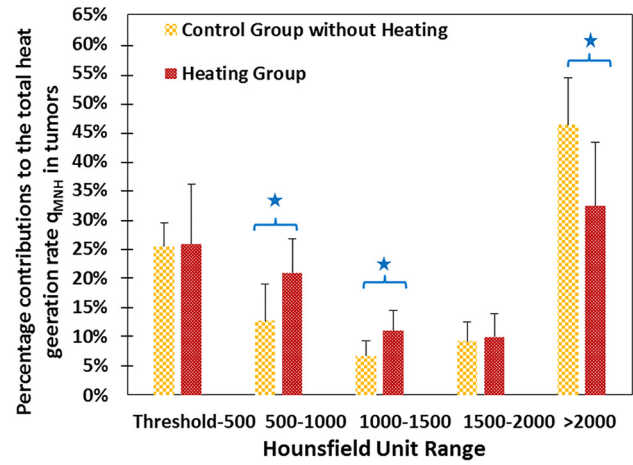


Fig. 8 Percentage of contribution of energy deposition rate in different Hounsfield unit ranges of the total energy generation rate in individual tumors. The symbol * denotes significant difference with a *p*-value less than 0.05 based on Student's *t*-test and Wilcoxon rank sum test.

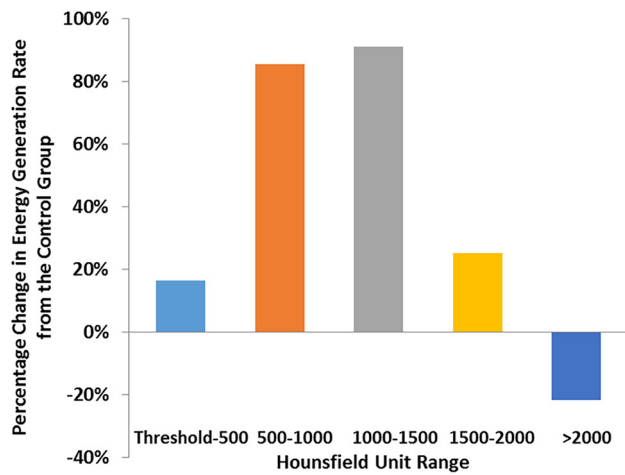


Fig. 7 Percentage change in energy generation rate in individual HU ranges from the control group tumors to the heating group tumors

q_{MNH}''' larger than 2.4×10^6 W/m³. Shown in both Table 1 and Fig. 6, in the control group without heating, among the average 0.35 W of the total heat generation rate in the tumor, 0.088 W is contributed by the nanoparticles in the lowest concentration range, while 0.163 W is from the nanoparticles in the highest concentration range. In the tumor group with heating, there are fewer nanoparticles in the highest concentration range, leading to only 0.127 W from the nanoparticles in the highest concentration range, which is 22% smaller than the control, illustrated in Fig. 7. The nanoparticles originally confined in the highest concentration range possibly migrated to lower concentration locations. As shown in Fig. 7, the energy deposition rate contributions from all the lower concentration ranges increase significantly, varying from 16% to 91% higher than the control. The *p*-values from

Student's *t*-test and Wilcoxon rank sum test are also given in Table 1. The determined *p*-values less than or close to 0.05 also confirmed statistical difference of change in most HU ranges between the control and heating groups.

Since the total amount of the energy generation rate varies slightly from one tumor to another, we then calculate the percentage of the heat generation rate contribution in specific HU ranges to the total heat generation rate in each tumor. The data are presented in Table 2 and illustrated in Fig. 8. The summation of the five columns from each group in Fig. 8 should be 100%. In the control group, more than 46% of the nanoparticles are deposited in the highly concentrated nanoparticle region with the HU values >2000, followed by 25% of the nanoparticles are in the lowest concentrated particle regions, with an HU in the range lower than 500. The percentage in the HU range larger than 2000 decreases significantly from 46% in the control to 32% in the heating group, while the percentages in the HU ranges of 500–1000, 1000–1500, and 1500–2000 in the heating group are much higher than that in the control group. The results shown in Fig. 8 again confirm the migration of nanoparticles from the highest concentration range to the lower concentration ranges. Statistical analyses using Student's *t*-test and Wilcoxon rank sum test have shown statistically significant change after heating with the *p*-value smaller than 0.05 in the HU ranges of 500–1000, 1000–1500, and >2000. For the HU range of 1500–2000, the average percentage in the heating group increase slightly from 9.1% in the control group to 9.9%, however, it failed to achieve a statistical difference. Similarly, no significant difference was found between the two groups in the HU range less than 500.

4 Discussion

This study focused on the evaluation of nanoparticle redistribution after heating treatment using magnetic nanoparticles as heat generators. Since the spatial distribution of nanoparticles in the tumor tissue determines the spatial temperature elevation during heating, it is imperative to precisely investigate whether the nanoparticles migrate from the central region to tumor periphery. The

Table 2 Percentage contributions of energy generation rates from individual HU ranges to the total energy generation rate

HU range	Threshold-500	500–1000 ^a	1000–1500 ^a	1500–2000	>2000 ^a
Control group	25.4 ± 4.1%	12.7 ± 6.2%	6.7 ± 2.5%	9.1 ± 3.4%	46.2 ± 7.9%
Heating group	25.8 ± 10.1%	20.9 ± 5.8%	11.0 ± 3.4%	9.9 ± 3.8%	32.4 ± 10.7%

^aDenotes significant difference between the control and heating group, *p* < 0.05, based on Student's *t*-test and Wilcoxon rank sum test.

information is not only crucial for designing an effective and safe heating protocol, but also useful when repeated heating strategy is needed. Demonstrated in our previous studies, microCT imaging is an excellent tool to visualize and quantify the density increase due to the presence of magnetic nanoparticles in tumor tissue, allowing quantification of nanoparticle distribution volume and energy deposition distribution in tumors. The previously determined relationship between the microCT HU value and the local nanoparticle concentration in tumors was implemented to further assess the volumetric heat generation rate in PC3 tumors. To the best of our knowledge, this was the first time when direct visualization and quantification of nanoparticle redistribution were demonstrated in PC3 tumor tissue. Similar to the results of our previous gel experiments, heating the tumor for 25 min resulted in a statistically significant increase in nanoparticle distribution volume of more than 42%. The nanoparticle distributions in both tumor groups can be imported to commercial software packages to simulate temperature elevation fields in those tumors, and to assess thermal damage. The designed heating protocols based on individual nanoparticle distribution in either the control group or the heating group can then be determined. Even if how the magnetic nanoparticles migrated during the 25 min of heating is unclear, the current results can be implemented to theoretically evaluate possible effect of different nanoparticle distributions on thermal dosage required to completely destroy PC3 tumors. Although this study focuses on the utilization of nanoparticle in hyperthermia for cancer treatment, the knowledge and understanding gained through this research may be applied to drug delivery in the same field. One challenge in drug delivery using nanocarriers is nanostructure transport barriers from tumor capillaries to tumor interstitial space in order to diffuse to the entire tumor region. Drug carrying nanoparticles are often accumulating in the vicinity of tumor capillaries due to their large sizes. It is essential to have a uniform drug concentration in tumors to damage not only the tumor vasculature, but also tumor cells. This study is the first step to provide understanding of deposition of nanomaterials in tumors and effective heating approaches to manipulate nanoparticle transports in cancer treatment.

Nanoparticle distribution in porous tumors is difficult to model since it involves complex processes including diffusion and advection of carrier solution in porous tissues, particle transport in solution, particle agglomeration, deposition of particle on tissue structure, and particle intake by cell and circulation. Particle size and shape, physical–chemical properties of the solution, and microstructure of tissue, as well as the dynamic response of nanostructures to heating during therapeutic treatments, could change nanoparticle distribution in tumors. Since the microCT image scan was taken in tumors before or after heating in this study, information of the nanoparticle migration process is not available to evaluate. Strong experimental evidence in this study has not only illustrated an overall nanoparticle distribution volume increase in the tumors after heating, but also suggested migration of the nanoparticles in the highest concentration region to the tumor region with a lower nanoparticle concentration. However, it is unclear what kinds of mechanisms resulted in the nanoparticle redistribution triggered by heating. We can only speculate possible factors that contribute to the observed particle migration. The heating protocol implemented in this study would lead to permanent thermal damage of the entire tumor, based on our previous *in vivo* experimental study on PC3 tumors implanted in mice [14]. When the tumor cells become necrotic, intracellular solution release from the dead cells may occur after the cell membrane is ruptured. This would lead to a significant increase in the interstitial volume fraction, φ_e . Considering the tumor tissue as a porous medium, one can write the diffusion coefficient of the nanoparticle, D_n , as a function of the interstitial space fraction using the following equation [27–28]:

$$D_n = \frac{2\varphi_e}{3 - \varphi_e} D_{n,f} \quad (3)$$

where $D_{n,f}$ is a nanoparticle diffusion coefficient in interstitial fluid. This equation suggests that when the interstitial space fraction increases from 20% in an unheated tumor to 60% after heating to completely damage the entire tumor, the diffusion coefficient could increase more than 3.5-fold. It is not clear whether the 3.5-fold increase in the diffusion coefficient is sufficient to cause the observed nanoparticle migration. Other factors, such as increased local blood perfusion rate may also play a significant role here. Blood perfusion rate can increase due to vasodilation of small arterials, and/or opening of capillaries originally closed. Delivery of a large blood flow to the tumor region can also be facilitated due to heating-reduced interstitial pressure decrease in the tumor center [14,29]. The large rise of local blood perfusion rate and decreased interstitial pressure would also strengthen the interstitial flow from the tumor center to the peripheral region and disperse the accumulated nanoparticles near in the vicinity of the injection center. We believe that the experimental results in this study can be used in future multiscale modeling approaches to evaluate contributions of these possible mechanisms on nanoparticle redistribution. Future experiments using better tools are also needed to illustrate the roles played by those mechanisms.

Another important factor can affect nanoparticle distribution in tumors is possible crack formation during an intratumoral injection process. The irregular distribution patterns of nanoparticle distribution in tumors observed in our previous studies strongly suggest small crack formation during the injection process [21]. Further, the distribution is more irregular when the injection rate is higher. In this study, we attempted to minimize crack formation via implementing a very slow injection rate of 3 $\mu\text{L}/\text{min}$. This injection rate was identified in our nanoparticle deposition after an intratumoral injection [7]. We also observed only minor or no nanofluid leakage from the injection site, via leaving the needle inside the tumor for 30 min after the injection ended. We were also very careful when resecting the tumors from the mouse bodies to minimize any loss of ferrofluid to the mouse body. These techniques seemed to have resulted in significant improvement over previous experiments when 11% to 50% of ferrofluid was reported to leak out from the tumor [21,30]. In addition, the calculated energy deposition rates from both the heated and unheated tumor groups also suggest minimal ferrofluid leakage. The total energy rates deposited in the tumors were very similar between the control group and the heating group. This is expected with no ferrofluid leakage, since all tumors were injected with the same amount of the same ferrofluid. The calculated total energy rates in both groups were also similar to that in our previous study [7], indicating repeatability of the experimental approach.

In this study, we used a previously determined relationship between the HU value and the volumetric heat generation rate when the magnetic nanoparticles are subject to an alternating magnetic field of 5 kA/m. The value of the magnetic strength at the center of the coils was estimated rather than measured. It is unclear to us whether the magnetic field was uniform within the volume of the tumor, although the tumor was very small compared to the diameter of the coils. As pointed out by previous studies [31], development of a uniform alternating magnetic field to cover a large treatment volume is important for reliable thermal treatment design. Another limitation of the study is on the accuracy of the volumetric heat generation calculation based on the linear portion of the temperature rising curve in our previous study. This method is based on the assumption that the temperature field within the specimen is sufficiently uniform to neglect heat conduction from the sample center to its boundary during heating. In reality, this assumption is difficult to satisfy precisely. Other methods are available to fit the temperature rising curve. One of them is the Box–Lucas model assuming that the temperature rising curve with time t can be described by an exponential function as

$$T(t) = A(1 - e^{-Bt}) \quad (4)$$

This model describes correctly the initial linear portion of the temperature rise with a slope as $A \cdot B$, but also the later influence of the heat conduction due to the nonuniform temperature as time passes. The Box–Lucas model has been used in past to quantify specific loss power or specific absorption rate of the heat generation rate due to magnetic nanoparticles [32,33]. It may be more accurate than the approach of our previous study since it does not require decision on what portion of the rising curve is used to fit a linear curve.

The calibrated relationship of the volumetric heat generation rate is based on the assumption of no nanoparticle agglomeration in tumors. Recent papers [34,35] have suggested that nanoparticles may agglomerate in phosphate-buffered saline, agarose gels, or suspensions containing cells, leading to a decreased q''_{MNH} value from that in its original ferrofluid concentration. It even showed a decrease in magnetic relaxation time with increasing nanoparticle concentration when the concentration exceeded a certain level [36]. In previous studies by our group, using the same calibrated relationship to design a heating protocol and later implementing the heating protocol to PC3 tumors have demonstrated good agreement between theoretical prediction and experimental study on tumor damage, implying acceptable accuracy of the calibration curve [14]. However, future experimental studies with imaging tools are needed to evaluate whether nanoparticles agglomerate in tumor tissue, although quantification of q''_{MNH} of magnetic nanoparticles in tumor tissue would be difficult due to nonuniform distribution of nanoparticles in tissue.

It would have been ideal to test our hypothesis using the same tumor in both the control and heating groups. The implanted tumor can be injected with ferrofluid, and scanned by microCT with the mouse anaesthetized. The tumor on the mouse can then be heated for 25 min. After the heating, the same tumor can be scanned again to see whether nanoparticle distribution is changed. Unfortunately, our microCT system does not allow in vivo animal scan. We have to rely on statistical analyses to determine whether heating truly induces nanoparticle redistribution in PC3 tumors, based on the large sample sizes of both the control and heating groups of PC3 tumors. The p -values are found to be less than 0.05 in either nanoparticle distribution volume or deposited energy generation rate in most HU ranges. It adds confidence to draw a conclusion that local heating-induced nanoparticle redistribution. In addition to microCT scan, in the future, other complementary methods such as histologic analyses of the tumors should also been used to confirm nanoparticle spreading due to local heating.

In summary, in vivo animal experiments were performed on PC3 tumors implanted in mice to investigate whether local heating via exposing the tumor to an alternating magnetic field (5 kA/m and 192 kHz) for 25 min resulted in nanoparticle spreading from the intratumoral injection site. Nanoparticle redistribution due to local heating is evaluated via comparing microCT images of resected tumors after heating to those in the control group without heating. A previously determined calibration relationship between microCT HU values and local nanoparticle concentrations in the tumors was used to determine the distribution of volumetric heat generation rate when the nanoparticles were subject to an alternating magnetic field. Analyses were performed to determine the total heat generation rate and the nanoparticle distribution volumes in individual HU ranges. Compared to the tumors in the control group, nanoparticles in the tumors in the heating group occupied not only the vicinity of the injection site, but also tumor periphery. We conclude that heating PC3 tumors for 25 min resulted in significant nanoparticle migration from highly concentrated regions to low concentration regions in the tumors. The volumetric heat generation rate distribution based on nanoparticle distribution before or after local heating can be used in the future to guide simulation of nanoparticle redistribution and its induced temperature rise in PC3 tumors during magnetic nanoparticle hyperthermia, therefore, accurately predicting required thermal dosage for safe and effective thermal therapy.

Acknowledgment

The research was performed in partial fulfillment by Qimei Gu of the requirements for the Ph.D. degree from the University of Maryland Baltimore County.

Funding Data

- National Science Foundation (CBET-1705538, Funder ID. 10.13039/100000001).

References

- [1] Espinosa, A., Di Corato, R., Kolosnjaj-Tabi, J., Flaud, P., Pellegrino, T., and Wilhelm, C., 2016, "Duality of Iron Oxide Nanoparticles in Cancer Therapy: Amplification of Heating Efficiency by Magnetic Hyperthermia and Photothermal Bimodal Treatment," *ACS Nano*, **10**(2), pp. 2436–2446.
- [2] Hoopes, P. J., Mazur, C. M., Osterberg, B., Song, A., Gladstone, D. J., Steinmetz, N. F., Veliz, F. A., Bursey, A. A., R. J., and Fiering, S. N., 2017, "Effect of Intra-Tumoral Magnetic Nanoparticle Hyperthermia and Viral Nanoparticle Immunogenicity on Primary and Metastatic Cancer," *Proc. SPIE Int. Soc. Opt. Eng.* (epub).
- [3] LeBrun, A., and Zhu, L., 2018, "Magnetic Nanoparticle Hyperthermia in Cancer Treatment: History, Mechanism, Imaging-Assisted Protocol Design, and Challenges," *Theory and Application of Heat Transfer in Cells and Organs*, S. Devashish, ed., Wiley, Hoboken, NJ, pp. 758–776.
- [4] Maier-Hauff, K., Ulrich, F., Nestler, D., Niehoff, H., Wust, P., Thiesen, B., Orawa, H., Budach, V., and Jordan, A., 2011, "Efficacy and Safety of Intratumoral Thermotherapy Using Magnetic Iron-Oxide Nanoparticles Combined With External Beam Radiotherapy on Patients With Recurrent Glioblastoma Multiforme," *J. Neuro-Oncol.*, **103**(2), pp. 317–324.
- [5] Petryk, A. A., Misra, A., Mazur, C. M., Petryk, J. D., and Hoopes, P. J., 2015, "Magnetic Nanoparticle Hyperthermia Cancer Treatment Efficacy Dependence on Cellular and Tissue Level Particle Concentration and Particle Heating Properties," *Proc. SPIE*, **9326**, p. 93260L.
- [6] Dähring, H., Grandke, J., Teichgräber, U., and Hilger, H., 2015, "Improved Hyperthermia Treatment of Tumors Under Consideration of Magnetic Nanoparticle Distribution Using Micro-CT Imaging," *Mol. Imaging Biol.*, **17**(6), pp. 763–769.
- [7] LeBrun, A., Joglekar, T., Bieberich, C., Ma, R., and Zhu, L., 2016, "Identification of Infusion Strategy for Achieving Repeatable Nanoparticle Distribution and Quantifiable Thermal Dosage in Magnetic Nanoparticle Hyperthermia," *Int. J. Hyperthermia*, **32**(2), pp. 132–143.
- [8] Pennes, H. H., 1948, "Analysis of Tissue and Arterial Blood Temperature in the Resting Human Forearm," *J. Appl. Physiol.*, **1**(2), pp. 93–122.
- [9] Song, C. W., 1984, "Effect of Local Hyperthermia on Blood Flow and Microenvironment: A Review," *Cancer Res.*, **44**(Suppl. 10), pp. 4721–4730.
- [10] Lang, J., Erdmann, B., and Seebass, M., 1999, "Impact of Nonlinear Heat Transfer on Temperature Control in Regional Hyperthermia," *IEEE Trans. Biomed. Eng.*, **46**(9), pp. 1129–1138.
- [11] Rodrigues, H. F., Capistrano, G., Mello, F. M., Zufelato, N., Silveira-Lacerda, E., and Bakuzis, A. F., 2017, "Precise Determination of the Heat Delivery During In Vivo Magnetic Nanoparticle Hyperthermia With Infrared Thermography," *Phys. Med. Biol.*, **62**(10), pp. 4062–4082.
- [12] Rylander, M. N., Feng, Y., Zhang, Y., Bass, J., Stafford, R. J., Volgin, A., Hazle, J. D., and Diller, K. R., 2006, "Optimizing Heat Shock Protein Expression Induced by Prostate Cancer Laser Therapy Through Predictive Computational Models," *J. Biomed. Opt.*, **11**(4), p. 041113.
- [13] LeBrun, A., Ma, R., and Zhu, L., 2016, "MicroCT Image Based Simulation to Design Heating Protocols in Magnetic Nanoparticle Hyperthermia for Cancer Treatment," *J. Therm. Biol.*, **62**, pp. 129–137.
- [14] LeBrun, A., Joglekar, T., Bieberich, C., Ma, R., and Zhu, L., 2017, "Treatment Efficacy for Validating MicroCT Based Theoretical Simulation Approach in Magnetic Nanoparticle Hyperthermia for Cancer Treatment," *ASME J. Heat Transfer*, **139**(5), p. 051101.
- [15] Jordan, A., Scholz, R., Wust, P., Fähling, H., Krause, J., Włodarczyk, W., Sander, B., Vogl, T., and Felix, R., 1997, "Effects of Magnetic Fluid Hyperthermia (MFH) on C3H Mammary Carcinoma In Vivo," *Int. J. Hyperthermia*, **13**(6), pp. 587–605.
- [16] Winslow, T. B., Eranki, A., Ullas, S., Singh, A. K., Repasky, E. A., and Sen, A., 2015, "A Pilot Study of the Effects of Mild Systemic Heating on Human Head and Neck Tumour Xenografts: Analysis of Tumour Perfusion, Interstitial Fluid Pressure, Hypoxia and Efficacy of Radiation Therapy," *Int. J. Hyperthermia*, **31**(6), pp. 693–701.
- [17] Ma, R., Su, D., and Zhu, L., 2012, "Multiscale Simulation of Nanoparticle Transport in Deformable Tissue During an Infusion Process in Hyperthermia Treatments of Cancer," *Nanoparticle Heat Transfer and Fluid Flow, Computational & Physical Processes in Mechanics & Thermal Science Series*, Vol. 4, W. J. Minkowycz, E. Sparrow, and J. P. Abraham, ed., CRC Press, Taylor & Francis Group, Boca Raton, FL.
- [18] Neeves, K. B., Sawyer, A. J., Foley, C. P., Saltzman, W. M., and Olbricht, W. L., 2007, "Dilation and Degradation of the Brain Extracellular Matrix Enhances Penetration of Infused Polymer Nanoparticles," *Brain Res.*, **1180**, pp. 121–132.

- [19] Su, D., Ma, R., Salloum, M., and Zhu, L., 2010, "Multi-Scale Study of Nanoparticle Transport and Deposition in Tissues During an Injection Process," *Med. Biol. Eng. Comput.*, **48**, pp. 853–863.
- [20] Tien, C., and Ramarao, B. V., 2007, *Granular Filtration of Aerosols and Hydrosols*, 2nd ed., Elsevier, Oxford, UK.
- [21] Attaluri, A., Ma, R., Qiu, Y., Li, W., and Zhu, L., 2011, "Nanoparticle Distribution and Temperature Elevations in Prostate Tumors in Mice During Magnetic Nanoparticle Hyperthermia," *Int. J. Hyperthermia*, **27**(5), pp. 491–502.
- [22] Gu, Q., Min Zaw, M., Munuhe, T., Ma, R., and Zhu, L., 2017, "Nanoparticle Re-Distribution in Tissue-Equivalent Gels Induced by Magnetic Nanoparticle Hyperthermia," Summer Biomechanics, Bioengineering, and Biotransport Conference, Tucson, AZ, June 21–24, Paper No. 17-A-713-SB3C.
- [23] Zhang, K., and Waxman, D. J., 2010, "PC3 Prostate Tumor-Initiating Cells With Molecular Profile FAM65B^{high}/MF12^{low}/LEF1^{low} Increase Tumor Angiogenesis," *Mol. Cancer*, **9**(1), pp. 319–332.
- [24] Manuchehrabadi, N., Attaluri, A., Cai, H., Edziah, R., Lalanne, E., Bieberich, C., Ma, R., Johnson, A. M., and Zhu, L., 2013, "Tumor Shrinkage Studies and Histological Analyses After Laser Photothermal Therapy Using Gold Nanorods," *J. Biomed. Eng. Technol.*, **12**(2), pp. 157–176.
- [25] Mah, P., Reeves, T. E., and McDavid, W. D., 2010, "Deriving Hounsfield Units Using Grey Levels in Cone Beam Computed Tomography," *Dentomaxillofac. Radiol.*, **39**(6), pp. 323–335.
- [26] Urata, M., Kijima, Y., Hirata, M., Shinden, Y., Arima, H., Nakajo, A., Koriyama, C., Arigami, T., Uenosono, Y., Okumura, H., Maemura, K., Ishigami, S., Yoshinaka, H., and Natsugoe, S., 2014, "Computed Tomography Hounsfield Units Can Predict Breast Cancer Metastasis to Axillary Lymph Nodes," *BMC Cancer*, **14**, p. 730.
- [27] El-Kareh, A. W., Braunstein, S. L., and Secomb, T. W., 1993, "Effect of Cell Arrangement and Interstitial Volume Fraction on the Diffusivity of Monoclonal Antibodies in Tissue," *Biophys. J.*, **64**(5), pp. 1638–1646. [8324199]
- [28] Zhang, A., Mi, X., Yang, G., and Xu, L. X., 2009, "Numerical Study of Thermally Targeted Liposomal Drug Delivery in Tumor," *ASME J. Heat Transfer*, **131**(4), p. 043209.
- [29] Roh, H. D., Boucher, Y., Kaliniki, S., Buchsbaum, R., Bloomer, W. D., and Jain, R. K., 1991, "Interstitial Hypertension in Cervical Carcinomas in Humans: Possible Correlation With Tumor Oxygenation and Radiation Response," *Cancer Res.*, **51**(24), pp. 6695–6698.
- [30] Johannsen, M., Gneveckow, U., Thiesen, B., Taymoorian, K., Cho, C. H., Waldofner, N., Scholz, R., Jordan, A., Lowning, S. A., and Wust, P., 2007, "Thermotherapy of Prostate Cancer Using Magnetic Nanoparticles: Feasibility, Imaging, and Three-Dimensional Temperature Distribution," *Eur. Urol.*, **52**(6), pp. 1653–1662.
- [31] Attaluri, A., Nusbaum, C., Wabler, M., and Ivkov, R., 2013, "Calibration of a Quasi-Adiabatic Magneto-Thermal Calorimeter Used to Characterize Magnetic Nanoparticle Heating," *ASME J. Nanotechnol. Eng. Med.*, **4**, p. 011006.
- [32] Bordelon, D. E., Cornejo, C., Gruttner, C., Westphal, F., DeWeese, T. L., and Ivkov, R., 2011, "Magnetic Nanoparticle Heating Efficiency Reveals Magneto-Structural Differences When Characterized With Wide Ranging and High Amplitude Alternating Magnetic Fields," *J. Appl. Phys.*, **109**(12), p. 124904.
- [33] Landi, G. T., 2013, "Simple Models for the Heating Curve in Magnetic Hyperthermia Experiments," *J. Magn. Magn. Mater.*, **326**, pp. 14–21.
- [34] Etheridge, M. L., Hurley, K. R., Zhang, J., Jeon, S., Ring, H. L., Hogan, C., Haynes, C. L., Garwood, M., and Bischof, J. C., 2014, "Accounting for Biological Aggregation in Heating and Imaging of Magnetic Nanoparticles," *Technology*, **2**(3), pp. 214–228.
- [35] Jeon, S., Hurley, K. R., Bischof, J. C., Haynes, C. L., and Hogan, C. J., 2016, "Quantifying Intra- and Extracellular Aggregation of Iron Oxide Nanoparticles and Its Influence on Specific Absorption Rate," *Nanoscale*, **8**(35), pp. 16053–16064.
- [36] Deatsch, A., and Evans, B. A., 2014, "Heating Efficiency in Magnetic Nanoparticle Hyperthermia," *J. Magn. Magn. Mater.*, **354**, pp. 163–172.